Available online at www.sciencedirect.com

ScienceDirect

Procedia CIRP 00 (2022) 000–000

www.elsevier.com/locate/procedia

12th CIRP Conference on Photonic Technologies [LANE 2022], 4-8 September 2022, Fürth, Germany

A multi-physics CFD study on the part-to-part gap during remote laser welding of copper-to-steel battery tab connectors with beam wobbling

Giovanni Chianese[a]*, Sharhid Jabar[b], Pasquale Franciosa[b], Dariusz Ceglarek[b], Stanislao Patalano[a]

[a]*Department of Industrial Engineering, University of Naples Federico II, P.le Tecchio 80, Naples 80125, Italy*
[b]*WMG, The University of Warwick, 6 Lord Bhattacharyya Way, Coventry, CV4 7AL, United Kingdom*

* Corresponding author. *E-mail address:* giovanni.chianese@unina.it

Abstract

Remote Laser Welding (RLW) of dissimilar metallic thin foils (below 500 µm) has fundamental importance in battery pack manufacturing where high repeatability is a strict requirement. Since the welding process is very sensitive to part-to-part gaps, it is critical to understand the physical phenomena during melting, formation of the keyhole and solidification. This study has been designed to investigate the underlying physics of the welding process and understand the influence of the laser beam wobbling and part-to-part gap on temperature fields and metal mixing. A CFD multi-physics model has been implemented and then calibrated with experimental data. Two scenarios with part-to-part gap (0 and 100 µm) have been considered during lap welding of 300 µm copper to 300 µm nickel-plated steel, with circular beam wobbling. The study has highlighted that the part-to-part gap leads to uncontrolled metal mixing. Potential strategies for weld optimization are discussed throughout the paper.

Keywords: battery pack manufacturing; remote laser welding; CFD simulation; part-to-part gap; dissimilar metals & metal mixing; laser beam wobbling.

1. Introduction

There is common consensus that large scale electrification of transport represents one of the biggest disruptive technologies in decades [1]. It is estimated that laser-material processing covers between 60% to 80% of all material processing applications for Electric Vehicle (EV) manufacturing, and involves laser cutting, surface ablation/cladding and welding/bonding. With regards to welding technology, there is a growing interest in applying Remote Laser Welding (RLW) in battery manufacturing due to several advantages such as single sided non-contact access, reduced heat affected zone and processing time [2]. As the structure of a battery pack follows a pack-module-cell layout with battery cells clustered in modules and modules organized with series and parallel connections based on the desired power and capacity requirements [3], connections between cells have paramount importance. Joining of battery tab connectors involves various dissimilar thin foils (below 500 µm). Brandt et al. demonstrated that RLW is a suitable process for joining battery tab connectors since it allows to achieve the lowest electrical resistance and the highest joint strength, when compared to micro-spot welding and ultrasonic welding [4].

Repeatability of the welding process is paramount since connections resulting in unequal electrical resistances within the same battery pack result in uneven current loads that can reduce the overall electro-chemical performance of battery pack and lead to inhomogeneous cell degradation [2].

There are various challenges pertaining repeatability of the RLW process during joining of dissimilar thin foils. They include: *challenge 1* – manufacturing and clamping tolerances, which can generate an accumulated part-to-part gap of more than 100 µm and, thereby, lead to lack of joint connection; *challenge 2* - Inter Metallic Compounds (IMCs) can lead to formation of brittle structures with high electrical resistance, as reported in [5,6]; *challenge 3* – laser-material interaction and

coupling of the laser beam with the parent metals. Number of novel welding technologies have been developed and proposed in the literature to cope with challenge 3 – for example, novel laser system (i.e., visible lasers [7]) and/or beam shaping technologies (i.e., Adjustable Ring Mode laser [8]) which claim improved stability of the keyhole, and better coupling of the laser beam. Laser beam wobbling and pulsed lasers are also implemented to cope with high reflective materials, such as copper [9]. Challenge 1 and 2 are interdependent and most of the reported works have focused on investigating the effects of different welding parameters on the IMCs formation in the fusion zone, microstructure of joint materials, and mechanical properties. Only limited efforts were taken to understand the metal mixing in the welds subject to part-to-part gap. Ozkat et al. [10] developed a decoupled multi-physics model for prediction of the weld penetration and interface width during laser lap welding of zinc coated steel considering part-to-part gap. Drobniak et al. [11] and Buttazzoni et al. [12] implemented Computational Fluid Dynamics (CFD) multi-physics simulations of 1 mm-thick stainless-steel plates with part-to-part to optimize weld quality. Huang et al. [5] developed a CFD model in FLOW WELD® to study the metal mixing rate during RLW of 200 µm aluminum to 500 µm copper foils; however, the case with part-to-part gap was not considered.

This paper addresses challenge 1 and 2 and aims at investigating the effect of laser beam wobbling and part-to-part gap on temperature fields and metal mixing. A CFD multi-physics model has been developed and then calibrated with experimental data. Two scenarios with part-to-part gap (0 and 100 µm) have been considered during RLW of 300 µm copper to 300 µm nickel-plated steel, with circular beam wobbling. Calibration and validation of the model are performed via comparison of geometrical features, such as weld penetration depth and width of the weld seam at the top and at the interface between the foils.

Nomenclature

α	Accommodation coefficient (-)
γ	Ratio of specific heats of air (-)
ΔH_v	Latent heat vaporization (J/kg)
ρ	Mass density (kg/m^3)
σ	Surface tension (N/m)
∇_t	Gradient along tangent direction
c_v, c_p	Specific heat at constant volume/pressure (J/kg·K)
D	Diffusivity (m^2/s)
D_P	Penetration depth of the weld seam (µm)
f	Fraction of fluid (-)
k	Thermal conductivity (W/m·K)
l_{diff}	Extension of diffusion zone (m)
P_L	Laplace pressure
P_{sat}	Saturation pressure (Pa)
P_{vap}	Partial pressure exerted by vapour (Pa)
P_v, T_v	Coordinates of a point on the saturation curve (Pa, K)
R_I, R_{II}	Curvature radius at the interface (m)
Q_{mass}	Evaporation rate (kg/s)
t_{end}	Simulated welding time (s)
W_T , W_I	Weld width at the top and at the interface (µm)
Y	Species concentration (-)

2. Materials and methods

2.1. Materials and equipment

The RLW experiments consisted of 300 µm copper to 300 µm nickel-plated steel welded in overlap configuration with welding length of 30 mm. The size of the specimens was 50 mm x 30 mm. Edge effect was avoided by placing the start/end of the weld seam at 10 mm away from the edges of the specimens.

The employed laser unit was the nLight Compact Fiber Laser 3 kW (n-Light Inc., USA); the laser power was delivered to the specimens via a 2D F-theta scanner with telecentric lenses (Scout-200, Laser and Control K-lab, South Korea). Specifications of the equipment are reported in Table 1.

Table 1. Specifications of the welding equipment.

Compact Fiber Laser 3kW, nLight		Scout-200, K-lab	
Max. power	3 kW	Working field	70 x 70 mm^2
Wavelength	1070 ± 10 nm	Collimating length	160 mm
Beam quality	4 mm·rad	Focal length	254 mm
Fiber diameter	50 µm	Rayleigh length	0.8 mm

Circular laser beam wobbling was implemented with a wobbling radius of 0.2 mm and 500 Hz frequency; velocity of the linear motion was 120 mm/s. The laser power was delivered in continuous mode and no modulation, with a set value of 690 W. The position of the focal point was on the top surface of the copper foil. Shim packs (Meusburger GmbH, Germany) with 12.5 width were employed for controlling the part-to-part gap. Two part-to-part gaps were studied: 0 and 100 µm. All the experiments were performed without shielding gas nor filler wire.

Three cross sections (at 5 mm, 15 mm and 25 mm from the start of the weld) were taken in order to experimentally characterize the weld and calibrate the CFD model. Cross sections were grinded and polished (no etching) and, after mounting in resin disks, images were recorded by microscope Nikon Eclipse LV150N.

Calibration and validation of the CFD model was carried out by comparing the simulated weld profile to the experimental cross sections. Three geometrical features have been measured in each cross section (see Fig. 1): W_T is the width of the weld seam at the top surface; W_I is the width of the weld seam at the interface between the two foils measured on the steel side; and D_P is the maximum penetration in the steel foil. The error difference between experiments and simulation was calculated by averaging the values of geometrical features in the experimental cross sections. This allows taking into account the normal variations during the welding trials.

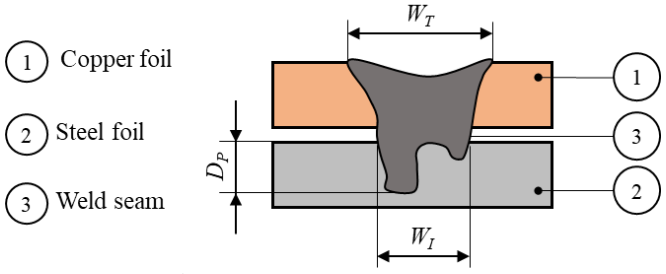

Fig. 1. Geometrical features measured in the cross-sections.

The mixing of parent metals was characterized by elemental mapping of the cross sections, performed with an FEI Versa 3D dual beam scanning electron microscope using Energy Dispersive X-ray Spectroscopy (EDS mapping).

2.2. Development of CFD model

The CFD multi-physics numerical model was developed using the commercial software FLOW-3D® and its module FLOW-WELD®. The following model assumptions were taken: (1) volumetric thermal expansion due to temperature dependent mass density is accounted; (2) the beam waste is assumed cylindrical – this is driven by the fact that the stacked thickness of the processed foils is within one Rayleigh length; (3) the laser beam is divided into a finite number of rays so that the tray-tracing model can be employed to track multiple reflections; (4) conduction heat sinking from the clamping mask is neglected since sufficient clearance (12 mm) was left between the weld seam and the mask itself; (5) vaporized metal and the air within the part-to-part gap is modelled as "void" - ambient temperature and pressure are assigned to the void for modelling the convective heat flux of the metal with the air (irradiance is neglected); (6) the liquid flow is regarded as Newtonian with incompressible liquid.

The computational domain consists of two nested meshes (Fig. 2): a fine mesh for the laser process zone and a coarse mesh for the thermal diffusion zone. The fine mesh domain was 4 mm long (this allows simulating an effective weld length of 3 mm with sufficient margin for the laser spot to transition from the coarse to the fine mesh), and 0.8 mm wide (this is sufficient to cover the full wobbling pattern of the laser beam). The thermal diffusion zone allows simulating a sub-region of the entire specimen and therefore reducing the computational complexity. Extension of the thermal diffusion zone, l_{diff}, was calculated based on equation (1) with a simulation time, t_{end}, equal to 0.026 s, corresponding to a 3 mm-long weld seam at 120 mm/s.

$$l_{diff} = 2\sqrt{2\frac{k(T=T_{amb})}{c_p(T=T_{amb})\cdot\rho(T=T_{amb})}t_{end}} \quad (1)$$

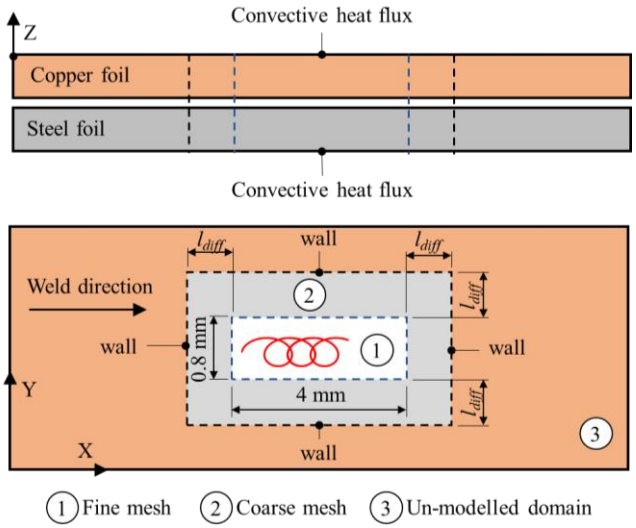

Fig. 2. Computational domain with nested meshes (l_{diff} = 4.9 mm).

Five different mesh sizes were considered: 40 µm, 20 µm, 15 µm, 10 µm and 5 µm. Mesh independent solution was achieved with mesh size of 15 µm and this led to approx. 1 million cells in the whole computational domain.

Boundary conditions were assigned as follow: (1) wall in the X and Y direction (with constant ambient temperature, T_{amb}); (2) natural convective heat flux in the Z direction, as the top and the bottom parts of the domain are in contact with air at ambient temperature.

The laser power distribution was measured with PRIMES power meter (Primes GmbH, Germany) and then modelled with a gaussian profile (nominal laser spot diameter on focus was 80 µm).

The following physics have been included in the model: fluid-flow via Navier-Stokes equations, continuity and energy conservation equation, evaporation and keyhole formation, solidification, species diffusion and conservation, Marangoni effect, and temperature-dependent absorption of the laser multiple reflections. Evaporation is modelled as mass transfer between liquid and void via coupling the vaporization equation (2) and the Clapeyron equation (3). During RLW process, intense vaporization increases the vapor pressure that tends to keep the keyhole open [15]. This pressure, known as recoil pressure, P_{recoil}, is accounted according to the formula in equation (4).

$$Q_{mass} = \frac{\alpha}{\sqrt{2\pi RT}}(P_{sat} - P_{vap}) \quad (2)$$

$$P_{sat} = P_v \cdot exp\left(\frac{\Delta H_v}{(\gamma-1)c_v T_v}\cdot\left(1-\frac{T_v}{T}\right)\right) \quad (3)$$

$$P_{recoil} = \alpha \cdot P_v \cdot exp\left(\frac{\Delta H_v}{(\gamma-1)c_v T_v}\cdot\left(1-\frac{T_v}{T}\right)\right) = A \cdot exp\left(B\cdot\left(1-\frac{T_v}{T}\right)\right) \quad (4)$$

The Volume-of-Fluid (VOF) method is implemented to track interfaces between liquid and void (gas). Equation (5) governs the VOF method and f and $\vec{V}$ are the fraction of liquid and the velocity field, respectively. The condition f = 0 indicates a cell with only void; values of f = 1 indicate a cell full of liquid; and the condition $0<f<1$ indicates the interface between liquid and void. Species conservation is modelled according to equation (6) to track the two parent metals (liquid of both copper and steel) and the metal mixing.

$$\frac{\partial f}{\partial t} + \nabla(\vec{V}f) = 0 \quad (5)$$

$$\frac{\partial}{\partial t}(\rho Y) + \nabla(\rho\vec{V}Y) = \nabla(D\rho\nabla Y) \quad (6)$$

$$P_L = \sigma\cdot\left(\frac{1}{R_I}+\frac{1}{R_{II}}\right) \quad (7)$$

$$S_M = \nabla_t\sigma \quad (8)$$

Besides the recoil pressure, surface tension has great influence on the process and is modelled as well. Surface tension determines two actions: the Laplace pressure P_L and the Marangoni force S_M. The Laplace pressure, P_L, is expressed by

equation (7) where σ, R_I and R_{II} are the surface tension and the curvature radii of the interface, respectively; the Marangoni force is caused by the gradient of the surface tension as expressed by equation (8), in which operator ∇_t indicates the gradient along the tangent direction to the interface.

Table 2. Material properties of adopted materials.

Property	Copper	Steel
Solidus temperature (K)	1357	1770
Liquidus temperature (K)	1358	1813
Latent heat of fusion (kJ/kg)	206.3	290
Vaporization temperature (K)	2835	3134
Latent heat of vaporization (MJ/kg)	4.727	6.080
Vapor specific heat (J/kg·K)	384.6	449

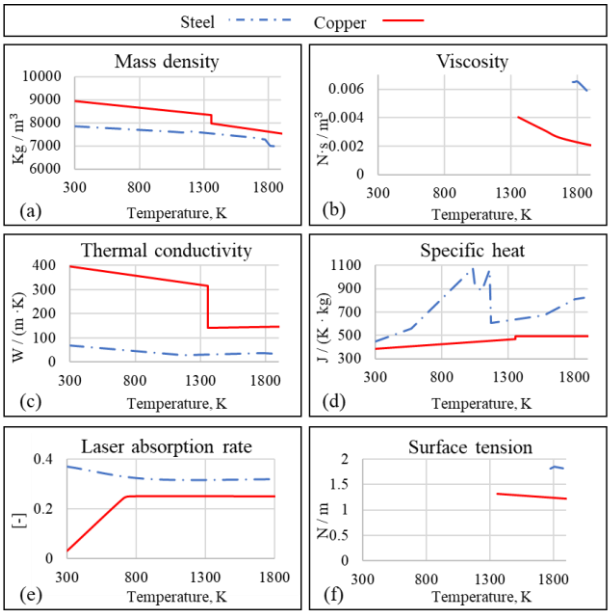

Fig. 3. Temperature-dependent material properties of copper (red solid line) and steel (blue dashed line).

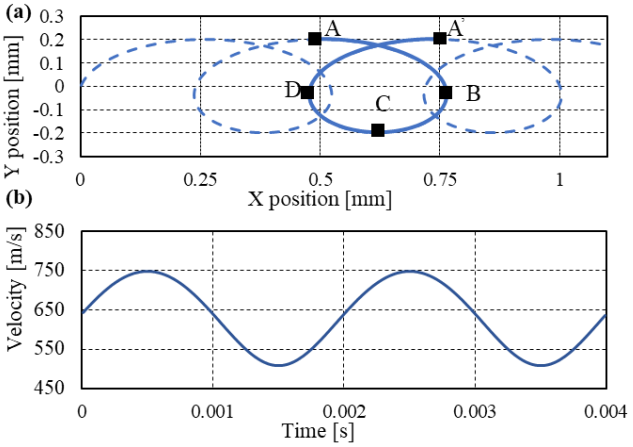

Fig. 4. (a) representation of the laser beam positions during a wobbling cycle; (b) velocity of the laser spot.

Table 3. Experimental vs. simulated geometrical features (values in µm).

	No part-to-part gap			Part-to-part gap = 100 µm		
	Experiment	Simulation	Diff.	Experiment	Simulation	Diff.
W_T	[504, 539]	[478, 504]	-5.8%	[510, 545]	[488, 518]	-4.6%
W_I	[274, 342]	[391, 425]	+32.5%	[142, 280]	[214, 254]	+10.9%
D_P	[183, 300]	[241, 259]	3.5%	[69, 133]	[77, 89]	-17.8%

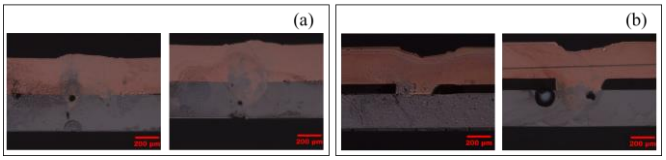

Fig. 5. Cross-sections (a) no part-to-part gap, and (b) 100 µm gap.

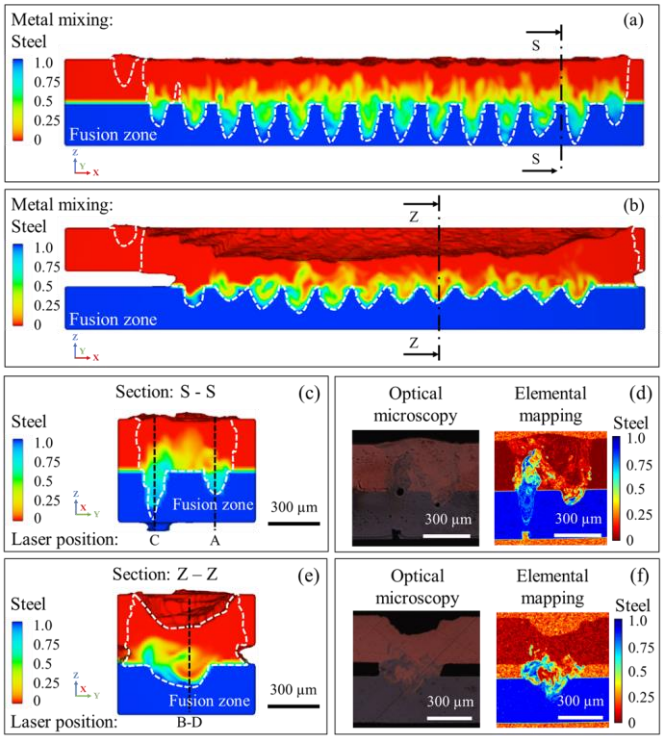

Fig. 6. Model validation and calibration. (a) Longitudinal section of the simulation in case of no gap, and, (b) 100 µm gap; (c) and (e) cross section of the simulated weld in case of no gap and 100 µm gap, respectively; (d) and (f) experimental cross sections (optical images) and elemental mapping in case of no gap and 100 µm gap, respectively.

3. Results and discussion

3.1. Model calibration and validation

Material properties (Table 2 and Fig. 3) were assumed temperature-dependent and were imported from the JMATPRO® material database. They were then calibrated to fit the experimental cross sections for both part-to-part gap scenarios (0 and 100 µm). Although the accommodation coefficients, α, of copper and steel are different they are treated with the same evaporation model in the CFD code. Therefore, the coefficient A in equation (4) was optimized to fit both materials.

Analysis of the cross sections showed that, due to the wobbling pattern of the laser spot (see Fig. 4) and no modulation of the laser power, a periodic waviness is observed in the weld profile (M-shaped profile). For instance, in both the part-to-part gap scenarios, the shape of the seam varies periodically between the two weld profiles shown in Fig. 5. This trend is well reproduced by the CFD simulations (Fig. 6 (a-b)).

Table 3 reports the comparison between experimental and simulated geometrical features. W_T and D_P are predicted with percentage error below 6% and 18%, respectively; whereas W_I

is overestimated in case of no gap. This is explained by the fact that the evaporation model is the same for both metals, and therefore the size of the keyhole is overestimated, especially at the copper-to-steel interface. Mixing mechanisms between parent metals are well reproduced in the simulations and are compatible with results of the EDS elemental mapping shown in Fig. 6 (d-f).

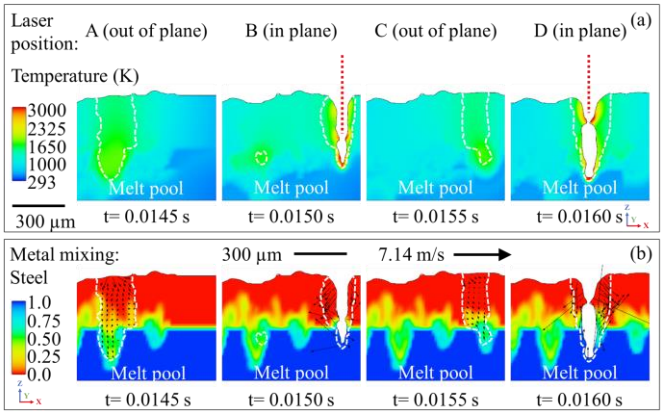

Fig. 7. (a) thermal field; and (b) metal mixing in the longitudinal section of the weld seam during a wobbling cycle (no part-to-part gap). Point B and D belong to the longitudinal section (in plane). A and C are out of plane.

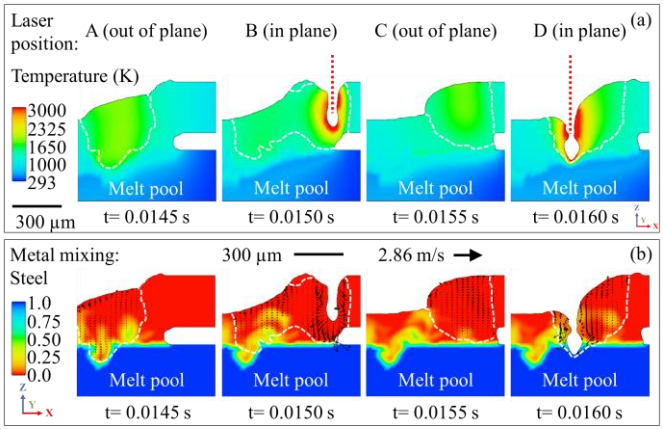

Fig. 8. (a) thermal field; and (b) metal mixing in the longitudinal section of the weld seam during a wobbling cycle (part-to-part gap = 100 µm). Point B and D belong to the longitudinal section (in plane). A and C are out of plane. *High resolution video*.

3.2. Main results and discussion

When comparing the results in Fig. 6 (a-b), it is clear that the part-to-part gap delays the bonding between the foils and influences the dynamics involved in the process. When the laser process starts, if the gap is zero (Fig. 6 (a)), the copper foil melts and transmits part of the heat to the adjacent steel foil, which behaves as heat sink; conversely, in case of part-to-part gap, the heat transfer from copper to steel is delayed due the presence of the gap, which acts as thermal barrier. Additionally, as the laser moves forward, the molten region on the copper side increases in size and is subject to three actions: (i) the gravity that causes motion of the molten copper towards the bottom determining contact with the steel foil; (ii) the internal friction due to viscosity forces that contrasts any motion and relative slips; and (iii) the surface tension with cohesive forces applied to the surface layer of the molten region. Only when the amount of molten copper increases, gravity prevails on viscous stresses and surface tension, and connection of the foils occurs, thus enabling gap bridging. Once the connection is established, the weld profile evolves and is characterized by a double dent/M-shaped.

The effect of beam wobbling and part-to-part gap is discussed below considering the four positions of the laser beam during a wobbling cycle defined in Fig. 4 (a), which are indicated as A, B, C and D.

- *Impact of wobbling pattern*: when the laser is in position A, its instant velocity is at maximum with minimum laser-material interaction time; whereas, when it is in position C, the velocity is at minimum, and the laser-material interaction time achieves its maximum. When the laser beam moves from position A to position C, the beam encounters un-processed material and this results in minimum weld penetration depth, which, in case of part-to-part gap, barely reaches the steel foil. When the laser beam moves from position C to A', the pre-processed material is molten again, and this results in maximum weld penetration depth. The wobbling pattern of the laser beam also influences the metal mixing. Variation of the laser beam velocity results in deeper penetration of the left dent and is associated with higher amount of molten material and higher temperatures, which promotes metal mixing. Diffusion of steel into the copper foil seems to be driven by buoyancy forces due to lower density of steel; conversely, mixing of copper into steel seems to be enhanced by the gravity due to higher density of copper (see Fig. 6 (c-e)).
- *Impact of part-to-part gap*: Fig. 7 and 8 show that the weld penetration depth is significantly lower in case of part-to-part gap. If the gap is zero (Fig. 7), the keyhole is established and extended to both the upper and lower foils, and, therefore, a sound connection is created. In case of part-to-part gap (Fig. 8), the results show that each cycle of the wobbling pattern can be divided in two phases: first, the laser warms up and melts unprocessed metal, which flows on the lower foil, and then, while the laser processes again the metal a connection between the two foils is established. Periodical connection between foils in the case of part-to-part gap matches well experimental results, as cross-sections with both sound weld and lack of connection have been observed within the same seam (Fig. 5). The impact on temperature fields and metal mixing is discussed as follows:
  - *Temperature field*: Fig. 7(a) and 8(a) show that the presence of part-to-part gap results in different thermal fields. The highest temperature is achieved on the keyhole walls, due to interaction with laser and multiple reflections, and the heat is transmitted to the surrounding metal. However, if there is no gap, direct contact between the two foils enhances heat transfer (Fig. 7(a)). In case of part-to-part gap, there is no direct contact between the two foils and the heat transfer is only ensured by the weld seam that bridges the gap; this results in lower temperatures in the steel foil (Fig. 8(a)).
  - *Metal mixing*: Fig. 7 (b) and 8 (b) show that different thermal fields result in different metal mixing mechanisms. Projected velocity fields are represented with black arrows and both recoil pressure and

temperature distribution seem to drive fluid flow. Arrows in the vicinity of the keyhole walls indicate that the recoil pressure drives the fluid from the bottom of the keyhole to the top and towards the outer region of the melt pool. The thermal gradient due to the rotation of the keyhole (consequence of the circular wobbling resulting in out-of-plane displacement) determines a flow that is represented with the projected velocity field. Fig. 7(b) (no gap) shows that the metal flow involves both copper and steel and enhances mixing throughout all the wobbling cycle in case of no gap. Fig. 8(b) (gap=100 µm) shows that the metal flow involves steel in a limited part of the wobbling cycle. This results in uncontrolled metal mixing and periodical discontinuity in the properties of the weld seam.

4. Conclusions and final remarks

This paper investigated the effect of laser beam wobbling and part-to-part gap (0 and 100 µm) on temperature fields and metal mixing during RLW of 300 µm copper to 300 µm nickel-plated steel. A combination of a CFD multi-physics model and experiments have been presented to shade some light on the metal mixing process. Moreover, the CFD model provided information about temperature fields, fluid flow and metal mixing, all of which are difficult to measure directly via physical experiments. Main findings are summarized as follows:

- Part-to-part gap delays the first connection between foils and is governed by surface tension, viscosity stress, and gravity force.
- Part-to-part gap limits heat transfer from the copper to the steel foil, resulting in lower temperatures in the steel and heat localization in the copper.
- When gap is zero, connection between foils is established throughout the whole wobbling cycle; whereas, in case of part-to-part gap, the connection is established periodically, since the laser penetrates only the upper foil during part of the wobbling cycle. This leads to uncontrolled metal mixing.
- The wobbling pattern and the sub-consequent periodic variation of laser beam velocity determines inhomogeneity in the metal mixing due to variation in the penetration depth, temperature fields and amount of molten metal.

Although the variation of part-to-part gap cannot be zeroed owing to manufacturing and clamping tolerances, its detrimental effect can be reduced by the welding process itself. Optimization of the process can be achieved via beam wobbling at higher frequency and/or power modulation. The combination of both techniques could help controlling the M-shaped weld profile and ultimately the metal mixing.

Future works will be devoted to weld process optimization with the support of the developed CFD model – this will include grain morphology optimization, characterization of IMCs and digital certification of electrical and mechanical properties to meet the requirements of battery pack design.

Acknowledgements

This study was financially supported by (1) WMG HVM Catapult; (2) APC UK project: ALIVE - Aluminium Intensive Vehicle Enclosures; (3) Innovate UK IDP15 project LIBERATE: Lightweight Innovative Battery Enclosures using Recycled Aluminium Technologies; and (4) Innovate UK FASA: Flexible, Automated Stator Assembly Platform for Lightweight Electric Motors. We acknowledge the technical support of Marcin Serdeczny (FLOW Science ®) and the contribution and support of the Student Exchange Program between University of Naples and The University of Warwick.

References

[1] Franciosa, P.; Sokolov, M.; Sun, T.; Chianese, G.; Ceglarek, D. ., 2021, “Laser Welding: High Volume Manufacturing for e-Mobility,” The Laser user, **M**(99), pp. 24–26.

[2] Chianese, G., Franciosa, P., Nolte, J., Ceglarek, D., and Patalano, S., 2021, “Characterization of Photodiodes for Detection of Variations in Part-To-Part Gap and Weld Penetration Depth During Remote Laser Welding of Copper-To-Steel Battery Tab Connectors,” Journal of Manufacturing Science and Engineering, **144**(July), pp. 1–34.

[3] Zwicker, M. F. R., Moghadam, M., Zhang, W., and Nielsen, C. V, 2020, “Journal of Advanced Joining Processes Automotive Battery Pack Manufacturing – a Review of Battery to Tab,” Journal of Advanced Joining Processes, **1**(March), p. 100017.

[4] Brand, M. J., Schmidt, P. A., Zaeh, M. F., and Jossen, A., 2015, “Welding Techniques for Battery Cells and Resulting Electrical Contact Resistances,” **1**, pp. 7–14.

[5] Huang, W., Wang, H., Rinker, T., and Tan, W., 2020, “Investigation of Metal Mixing in Laser Keyhole Welding of Dissimilar Metals,” Materials and Design, **195**, p. 109056.

[6] Perez Zapico, E., Ascari, A., Dimatteo, V., and Fortunato, A., 2021, “Laser Dissimilar Welding of Copper and Steel Thin Sheets for Battery Production,” Journal of Laser Applications.

[7] Wu, D., Zhang, P., Yu, Z., Gao, Y., Zhang, H., Chen, H., Chen, S., and Tian, Y. T., 2022, “Progress and Perspectives of In-Situ Optical Monitoring in Laser Beam Welding: Sensing, Characterization and Modeling,” Journal of Manufacturing Processes, **75**(November 2021), pp. 767–791.

[8] Sokolov, M., Franciosa, P., Sun, T., Ceglarek, D., and Dimatteo, V., 2021, “Applying Optical Coherence Tomography for Weld Depth Monitoring in Remote Laser Welding of Automotive Battery Tab Connectors,” Journal of Laser Applications.

[9] Mathivanan, K., and Plapper, P., 2019, “Laser Welding of Dissimilar Copper and Aluminum Sheets by Shaping the Laser Pulses,” Procedia Manufacturing, **36**, pp. 154–162.

[10] Ozkat, E. C., Franciosa, P., and Ceglarek, D., 2017, “Development of Decoupled Multi-Physics Simulation for Laser Lap Welding Considering Part-to-Part Gap,” Journal of Laser Applications, **29**(2), p. 022423.

[11] Drobniak, P., Otto, A., Vázquez, R. G., Arias, R. M., and Arias, J. L., 2020, “Simulation of Keyhole Laser Welding of Stainless Steel Plates with a Gap,” Procedia CIRP, **94**, pp. 731–736.

[12] Buttazzoni, M., Zenz, C., Otto, A., Gómez Vázquez, R., Liedl, G., and Arias, J. L., 2021, “A Numerical Investigation of the Laser Beam Welding of Stainless Steel Sheets with a Gap,” Applied Sciences (Switzerland), **11**(6).